

Top-down Segment-based Neuron Reconstruction

Anonymous CVPR submission

Paper ID 0446

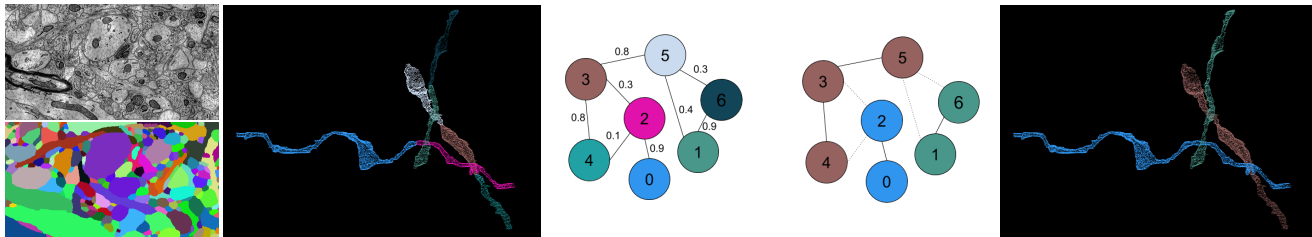


Figure 1: We take as input the results of a region-based agglomeration algorithm. We extract a graph from this segmentation and apply a top-down partitioning algorithm to improve accuracy.

Abstract

Advancements in electron microscopy image acquisition have created massive connectomics datasets which are petabytes in size and make manual segmentation infeasible. Proposed methods for automatic segmentations generate super-pixel approximations of neural membranes followed by agglomeration strategies to create full neuron reconstructions. However, pixel-based segmentation results widely neglect global geometric properties. We generate skeletons of membrane labels to approximate neural pathways in 3D. This allows us to efficiently apply graph-based optimization strategies and to train automatic classifiers for shape description against manually labeled ground truth. Our classifiers detect feasible and impossible neural pathways by looking at geometric properties alone, and are able to improve the segmentation labels accordingly. We demonstrate the performance of our classifiers on multiple real-world connectomics datasets with average variation of information improvement of $X\times$. We discuss our findings and provide insights to learning shape features for neuron agglomeration.

1. Introduction

The field of connectomics is concerned with reconstructing the wiring diagram of the brain at nanometer resolutions. Recent advancements in image acquisition using multi-beam serial-section electron microscopy (sSEM) has

allowed neuroscientists to produce terabytes of electron microscopy (EM) image data every hour [12]. Neuroscientists believe that reconstructing an entire mammalian brain at fine resolution will enable new insights into the workings of the brain [17]. These observations will allow for new advancements in neuromedicine and artificial intelligence.

Segmenting the image stack into a label volume is a substantial component of this reconstruction process. In a label volume, every voxel receives a segment label corresponding to a unique neuron. Voxels with the same label belong to the same neuron. It is not feasible for domain experts to manually segment the vast amount of 3-D image data to model an entire brain. Here we introduce a scalable, top-down segmentation algorithm that also leverages local information. Partitioning from a top-down approach allows us to apply domain-specific constraints to the segmentation task.

A significant amount of research focuses on automatic reconstruction of the neurons in EM images [21, 27, 29, 41]. All of these algorithms extract neuronal processes through the 3-D volumes using the raw image data as input. Oftentimes, convolutional neural networks (CNNs) predict membrane probabilities or affinities between voxels and apply simple thresholds to agglomerate the voxels into clusters [23, 31]. These *pixel-based* algorithms produce excellent results but currently fall short of complete reconstructions with error rates of approximately $X\%$.

Researchers address the failures of these pixel-based algorithms by training random-forest classifiers to agglomerate an oversegmentation of voxels [27, 28]. These classi-

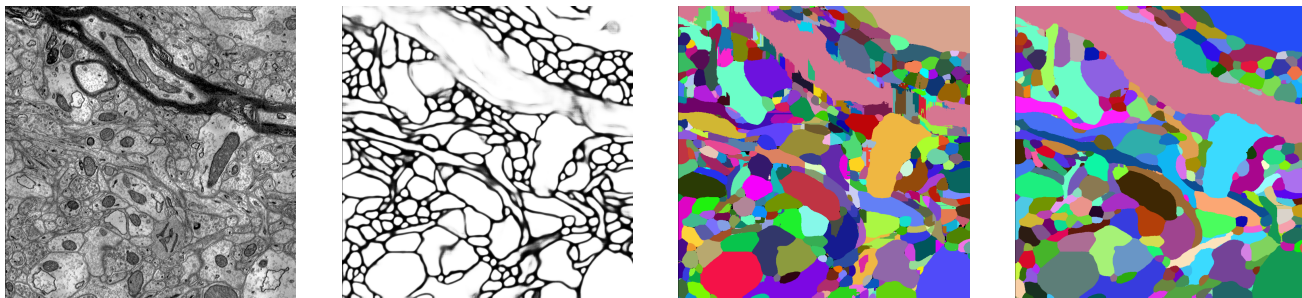


Figure 2: An overview of an existing pipeline in segmentation for connectomics. From left to right: the original EM image data, the output of a CNN predicting voxel affinities, clustering of the affinities using a watershed algorithm, an agglomeration of the supervoxels into larger segments.

fiers take the output of the pixel-based algorithms as input and generate high-level statistics such as affinity distributions between regions. Presently, these methods use hand-designed features despite the evidence that machine-learned features perform better [2]. These *region-based* algorithms outperform the pixel-based algorithms but do not provide the accuracy needed for large scale reconstructions of the brain.

We present a *segment-based* strategy that builds on the outputs of region-based methods (Figure 1). We only take as input a segmentation from the region-based agglomeration algorithm. This allows us to train on connectomics datasets at a given resolution and image type and test on another resolution. This is a huge plus considering the sheer amount of expert-hours needed to generate ground truth for these massive datasets. We extract a graph representation from the input segmentation. By simplifying the 3-D segments by their skeletons, we can quickly generate the graph nodes and edges. We train a 3-D CNN to populate the graph edge weights with bottom-up local information. We enforce domain-specific global constraints, such as the underlying biology, using a graph-based partitioning heuristic. In this we can leverage both local and global information to produce a more accurate segmentation.

Our novel approach creates a level of abstraction over existing region-based agglomeration strategies. We take the output of these methods as input and extract a graph structure from that. This allows us to enforce restrictions on our output that closely follow the underlying biology of these connectomics datasets. We use bottom-up information to weight the edges in our graph and top-down information when partitioning the graph. This dual approach of assessing local decisions in a global framework produces improvements over the existing region-based methods.

2. Related Work

A significant amount of research in computer vision focuses on the segmentation of images [39]. Here, we review

some of the most successful methods that have been applied to large-scale EM images. Figure 2 shows the results of a typical segmentation pipeline on these images.

Pixel-based methods. A large amount of connectomics research considers the problem of extracting segmentation information at the voxel level from the raw EM images to produce label volumes. Some early techniques apply computationally expensive graph partitioning algorithms with a single node per voxel [1], however these methods do not scale to terabyte datasets. Since then, several methods train 2-D CNNs to predict membrane probabilities per image slice [5, 14, 18, 22, 38]. More recent strategies augment these neural networks with the z -dimension creating full 3-D CNNs [23, 31]. Oftentimes these networks produce probabilities for the affinity between two voxels (i.e., the probability that adjacent voxels belong to the same neuron). The MALIS cost function is specifically designed for generating affinities that produce good segmentations [3]. More recently, flood-filling networks produce segmentations by training an end-to-end neural network that takes EM images to label volumes [15]. These flood-filling networks produce very impressive accuracies but at too high a computational cost.

Region-based methods. Several of these pixel-based approaches generate probabilities that neighboring voxels belong to the same neuron. Many algorithms build on top of these methods and train random-forest classifiers to produce segmentations of the EM images [21, 27, 28, 29, 41]. Despite the success of these classifiers, they often make mistakes based on the local information leading to errors in the segmentation. Lately, many recent advancements in segmentation use artificial neural networks since machine-learned features outperform hand-designed ones [2]. A significant amount of research focuses on the training and optimization of these deep neural networks [4, 24, 26].

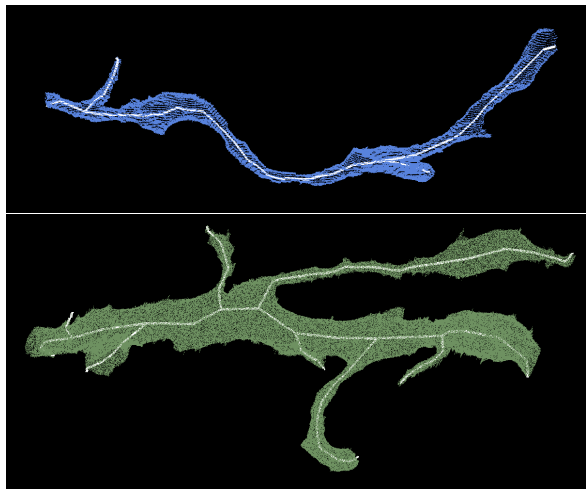


Figure 3: Skeletons using the TEASER algorithm.

Segment-based methods. Some limited research builds on top of the region-based methods to correct errors in the segmentation [30, 42, 10]. However, to our knowledge, we are the first to extract a graph representation from these region-based methods. Many segmentation and clustering algorithms use graph partitioning techniques [1] or normalized cuts for traditional image segmentation [16, 34, 36]. We can enforce domain-specific constraints using graph-based partitioning algorithms. Unfortunately graph partitioning is an NP-Hard problem [6]. However, there are several useful multicut heuristics which provide good approximations with reasonable computational costs [13, 20].

3. Method

There are two types of errors that can occur in image segmentation problems. The first, called a split error, occurs when there are two segments that should have been merged. The second, called a merge error, happens when one segment should be split into two. Generally, it is much more difficult to correct merge errors than to correct split errors (CITE). Our method takes as input an oversegmentation of an *EM* image volume where there are many more split errors than merge errors. Our goal is to identify locations of split errors and merge the corresponding segments. Section 4.1 discusses two pipelines for generating these segmentations.

From the input segmentation we generate a graph G with nodes N and edges E with weights w_e . The nodes correspond to label segments from the segmentation with edges between segments considered for merging. Ideally, our graph has edges corresponding to all of the segments which were erroneously split with few edges between correctly split segments. We generate a skeleton for every segment following the intuition that a skeleton represents

a simplified representation of the overall shape of an object. We locate merge candidates and produce corresponding edges based on these skeletons. A CNN generates the edge weights by learning a merge function given two segments as input. A multicut heuristic generates a partition on the graph where nodes in the same partition are assigned the same output label. Thus there are three major components to our framework: skeletonization for constructing a graph, network training for determining edge weights, and graph-partitioning using a multicut heuristic algorithm.

3.1. Graph Creation

We generate nodes N and edges E to apply a graph-based optimization strategy for segmentation. In addition, these edges receive non-negative weights.

3.1.1 Node Generation

The simplest node generation strategy creates one node for every unique segment label in the input volume. However, some of the millions of labels in the volume correspond to very small volumes. Usually these locations have noisy image data so the pixel-based methods could not provide enough information to generate a larger segment. It is difficult to extract useful shape features from these segments because of their small, and often random, shape. We prune these nodes from the graph by removing all segments with fewer than 20,000 voxels. This removes XX% of segments on a typical connectomics dataset.

3.1.2 Edge Generation

A naïve approach to generating edges produces an edge between all adjacent segments. Two segments l_1 and l_2 are considered adjacent if there is a pair of adjacent voxels where one has label l_1 and the other has label l_2 . NeuroProof and GALA consider all pairs of adjacent segments for merging. For us, this method produces too many edges in the graph. Therefore we present the following algorithm to identify pairs of segments to consider for merging.

First, we extract a skeleton from each segment using the TEASER algorithm [32, 40]. Figure 3 shows the skeletons in white of two segments from the label volume. These skeletons consist of a sequence of *joints*, locations that are a local maximum distance from the segment boundary, with line segments connecting successive joints. We prune the joints that are within 50 voxels of each other to reduce unnecessary branching. For the purposes of our algorithm, joints that have only one connected neighbor are referred to as *endpoints*. Many of the segments that are erroneously split follow a similar pattern (Figure 4). In these split instances the two skeletons have nearby endpoints.

After skeletonization, we begin to identify segments for merge consideration with the following two-pass heuristic.

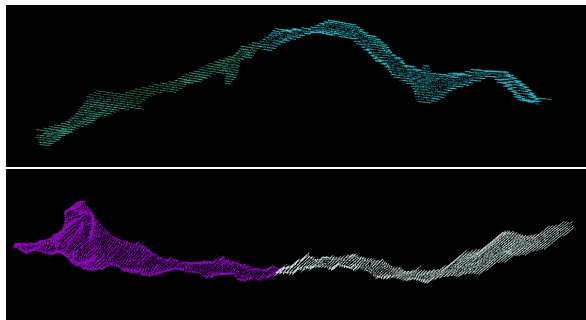


Figure 4: Two erroneously split segments.

In the first pass, we iterate over all endpoints e belonging to a segment S and create a set of segments \mathbb{S}'_e that includes all labels that have a single voxel within t_{low} voxels from e . Elements of these sets are candidates for merging. However the first pass often has too many candidates that should remain split so we apply an additional pass for further pruning. In the second pass, we consider all of the segments \mathbb{S}'_e for every endpoint e . If a segment $S' \in \mathbb{S}'_e$ has an endpoint within t_{high} voxels of e , the segment S and S' are considered for merging. We store the midpoint between the two endpoints as the “center” of the potential merge.

3.2. Edge Probabilities

The previous section outlines how to generate edges between nodes in our graph structure. Here we introduce a neural network architecture for generating probabilities that two nodes sharing an edge belong to the same neuron. The neural network takes as input only data from the input segmentation.

3.2.1 Network Architecture

Our graph generation algorithm produces 3-D locations that require further consideration for merging. To determine which of these segments should actually merge, we train a 3-D CNN using the oversegmentation and the corresponding manually labeled ground truth data (Section 4.1). We extract a cubic region of interest around these locations as input to the CNN. These regions of interest provide the local information for the neural network to predict which neighboring segments belong to the same neuron.

The networks receives three input channels for every voxel in the region of interest around segments l_1 and l_2 . The input to all of the channels is in the set $\{-0.5, 0.5\}$. The first channel is 0.5 only if the corresponding voxel has label l_1 . The second channel is 0.5 only if the corresponding voxel has label l_2 . The third channel is 0.5 if the corresponding voxel is either l_1 or l_2 .

Figure 5 provides an overview of our architecture. Our network architecture has three layers of double convolu-

tions followed by a max pooling step following the work of Chatfield et al. that found this technique improves on single convolution layers [4]. The first max pooling layer is anisotropic with pooling only in the x and y dimensions. The output after this final pooling step is flattened into a 1-D vector which is input into two fully connected layers. The final layer produces a probability with a sigmoid activation function [7]. All of the other activation functions are LeakyReLU [24]. We use a stochastic gradient descent optimizer with Nesterov’s accelerated gradient [26]. There are dropouts of 0.2 after every pooling layer and the first dense layer, and a dropout of 0.5 after the final dense layer to prevent overfitting. We discuss all other network parameters in Section 4.3.

3.3. Graph Partitioning

After constructing the graph structure we apply a graph-based segmentation strategy. There are many graph partitioning minimization functions that provide different constraints on their output. Neurons in the brain should be acyclic (i.e. the output shape should have a genus of zero). We enforce this constraint by finding a multicut partition of the graph that generates a *forest* on the nodes. A forest is a partitioning of a graph into a set of trees (i.e. no segment has a cycle). There are several heuristics that solve the multicut problem (which is NP-Hard). We use the greedy-additive algorithm [20].

4. Evaluation

We evaluate our schema on two different connectomics datasets, one anisotropic and the other isotropic, from two different species.

4.1. Datasets

Kasthuri. The Kasthuri dataset images the neocortex of a mouse brain produced by a scanning electron microscope [17]. This dataset is $5342 \times 3618 \times 338$ voxels in size. The resolution of the dataset is $3 \times 3 \times 30 \text{ nm}^3$ per voxel. We evaluate our methods using the left cylinder of this 3-cylinder dataset. We downsample the dataset in the x and y dimensions to give a final resolution of $6 \times 6 \times 30 \text{ nm}^3$ per voxel. We divide the dataset into two volumes along the x dimension. Thus, each volume is $8.0 \times 10.9 \times 10.1 \mu\text{m}^3$.

FlyEM. The FlyEM dataset comes from the mushroom body of a 5-day old adult male *Drosophila* fly imaged by a focused ion-beam milling scanning electron microscopy. The mushroom body in this species is the major site of associative learning [35]. The original dataset contains a $40 \times 50 \times 120 \mu\text{m}^3$ volume of which we use two cubes of size $10 \times 10 \times 10 \mu\text{m}^3$. The resolution of this dataset is $10 \times 10 \times 10 \text{ nm}^3$ so each volume has 1000 voxels in each dimension.

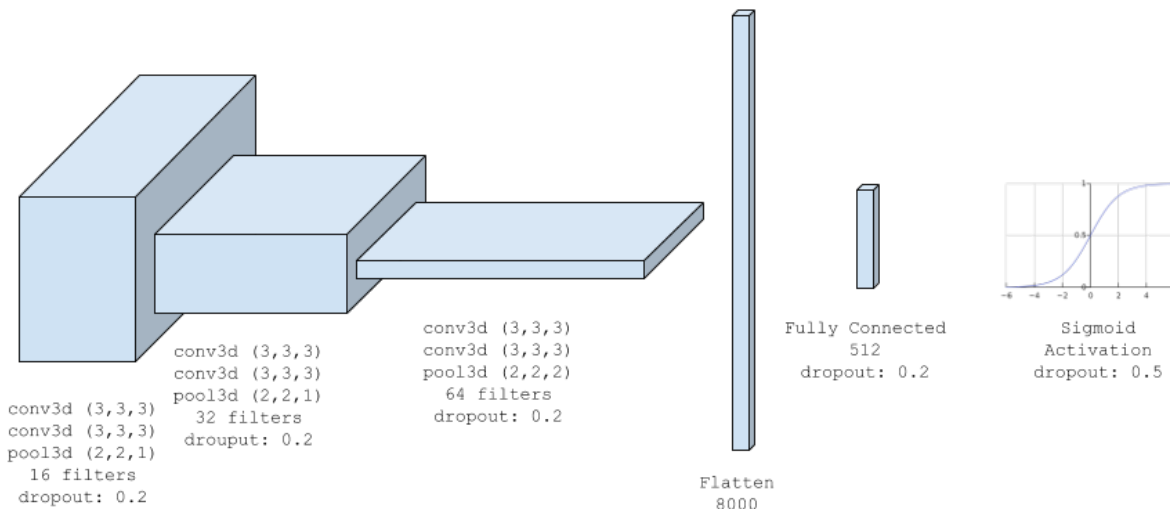


Figure 5: The architecture for the neural networks follows the VGG style of double convolutions followed by a max pooling operation. The number of filters doubles each layer leading to a fully connected layer and a sigmoid activation function.

Segmentation Pipeline and Baseline. The segmentation on the Kasthuri dataset was computed by agglomerating 3-D supervoxels produced by watershed from 3-D affinity predictions [41]. A recent study by Funke et.al. demonstrated superior performance of such methods over existing ones on anisotropic data [33]. We learned 3-D affinities using MALIS loss with a U-net [37, 31]. We apply the watershed algorithm, with suitable parameters, to compute a 3-D oversegmentation of the volume. The resulting 3-D oversegmentation is then agglomerated using the technique of context-aware delayed agglomeration to generate the final segmentation [28]. The variation of information (Section 4.5) values at different stopping thresholds of agglomeration correspond to the curve plotted in Figure 8.

We have collected two $1000 \times 1000 \times 1000$ voxel ($10 \times 10 \times 10 \mu\text{m}^3$) volumes from the authors [35]. Based on the authors' suggestion, we applied the context-aware delayed agglomeration algorithm [28] that shows improved performance on this dataset over the pipeline used in the original publication. This segmentation framework learns voxel and supervoxel classifiers with an emphasis to minimize undersegmentation error. At the same time this framework produces lower over-segmentation than standard algorithms. This algorithm first computes multi-channel 3-D predictions for membranes, cell interiors, and mitochondria, among other cell features. The membrane prediction channel is utilized to produce an oversegmented volume using 3-D watershed, which is then agglomerated hierarchically up to a certain confidence threshold. We used exactly the same parameters for the publicly available code for this algorithm and used different agglomerations thresholds to plot the variation of information error curve.

4.2. Pruning via Skeletonization

We prune potential merge candidates with the algorithm described in Section 3.1. There are two essential parameters to the algorithm: t_{low} and t_{high} . Ideally, the merge candidates output by this algorithm will contain all possible positive examples with a very limited number of negative examples. After considering various thresholds, we find that $t_{low} = 240 \text{ nm}$ and $t_{high} = 600 \text{ nm}$ produces the best results given this objective function. Note that these thresholds are in nanometers and not voxels. Connectomics datasets often have different sample resolutions and downsampling in z . Using nanometers allows us to have uniform units across all of these datasets and calculate the thresholds in voxels at runtime. The thresholds are $t_{low} = (40, 40, 8)$ voxels and $t_{high} = (100, 100, 20)$ voxels for the Kasthuri dataset and $t_{low} = (24, 24, 24)$ voxels and $t_{high} = (60, 60, 60)$ voxels for the FlyEM dataset. The thresholds are anisotropic or isotropic depending on the corresponding isotropy of the dataset. Table 2 shows the overall success of this method of candidate pruning.

4.3. Classifier Training

We use the Kasthuri Vol. 1 dataset for training and validation. We train on 80% of the potential merge candidates for this volume. We validate the neural network classifier on the remaining 20% of candidates. We consider networks with varying input sizes, optimizers, loss functions, filter sizes, learning rates, and activation functions. The supplemental material includes information on the experiments that determined these final parameters. Table 1 provides the parameters in the final network. There are 7,294,705 learn-

able parameters in our final architecture. All the parameters are randomly initialized following the Xavier uniform distribution [8]. Training concluded after 34 epochs.

Parameters	Values
Loss Function	Mean Squared Error
Optimizer	SGD with Nesterov Momentum
Momentum	0.9
Initial Learning Rate	0.01
Decay Rate	$5 * 10^{-8}$
Activation	LeakyReLU ($\alpha = 0.001$)
Kernel Sizes	$3 \times 3 \times 3$
Filter Sizes	$16 \rightarrow 32 \rightarrow 64$

Table 1: Parameters for the CNN

Data Augmentation. We apply data augmentation to the generated examples to increase the size of the training datasets. We consider all rotations of 90 degrees along the xy -plane in addition to mirroring along the x and z axes. This produces 16 times more training data.

4.4. Graph-based Strategies

Applying a top-down globally optimal partitioning function allows us to enforce some domain-specific constraints on the reconstruction. In connectomics, we want to enforce the topological restrictions that each partition in the graph has a genus of zero. The greedy-additive heuristic solves the multicut graph partitioning problem by enforcing this constraint. Previous agglomeration strategies at the per-region level consider neighboring superpixels in order of merge probability. These superpixels are clustered hierarchically without concern for global constraints. We compare the benefits of a top-down partitioning function versus the traditional bottom-up clustering methods.

4.5. Variation of Information

We evaluate the performance of our methods using the split version of variance of information [25]. Consider a ground truth labeling GT and our automatically reconstructed segmentation SG . Over and undersegmentation are quantified by the conditional entropy $H(GT|SG)$ and $H(SG|GT)$ respectively. Since we are measuring the entropy between two clusterings, better split variation of information scores are closer to the origin.

5. Results

5.1. Pruning via Skeletonization

Table 2 shows the results of pruning using the skeletonization heuristic. The baseline algorithm considers all

Dataset	Baseline	After Pruning
Kasthuri Vol. 1	763 / 21242 (3.47%)	753 / 3459 (17.88%)
Kasthuri Vol. 2	1010 / 26073 (3.73%)	904 / 4327 (17.28%)
FlyEM Vol. 1	269 / 14875 (1.78%)	262 / 946 (21.69%)
FlyEM Vol. 2	270 / 16808 (1.58%)	285 / 768 (27.07%)

Table 2: The results of our pruning heuristic compared to the current baseline.

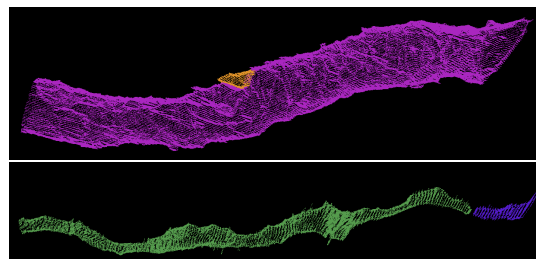


Figure 6: Example merge candidates.

Dataset	Precision	Recall	Accuracy
Kasthuri Training	0.919	0.936	0.974
Kasthuri Testing	0.737	0.717	0.907
FlyEM Vol. 1	0.796	0.478	0.862
FlyEM Vol. 2	0.762	0.422	0.810

Table 3: Precision and recall for the training and three test datasets.

adjacent regions for merging. Our method removes a significant portion of these candidates while maintaining a large number of the true merge locations. This edge pruning is essential for the graph partitioning algorithm which has a computational complexity dependence on the number of edges. Our pruning heuristic removes at least $6 \times$ the number of edges between correctly split segments on all datasets, achieving a maximum removal ratio of $20 \times$. Equally important is the number of split errors that remain after pruning. These are the locations that we want to merge to create a more accurate reconstruction. For every dataset, the number of positive candidates remains relatively even. However, since our heuristic does not enforce an adjacency constraint of two regions when constructing edges in the graph, the difference does not indicate the number of examples excluded by pruning. In fact, our method finds a number of examples which are non-adjacent. Figure 6 shows two example segments which are split errors. The top example our algorithm missed but the segments are adjacent. The bottom example our algorithm found despite the fact that they are not adjacent.

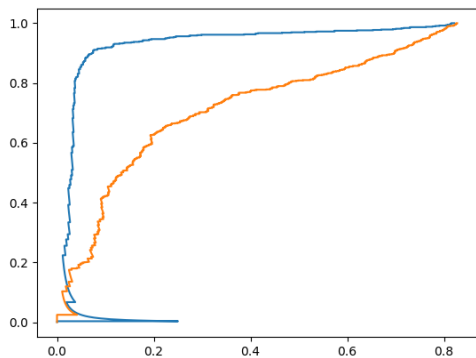


Figure 7: (NOT CORRECT) The receiver operating characteristic (ROC) curve for all four datasets.

5.2. Classification Performance

Table 3 shows the precision and recall for all of the datasets. Since, our method does not rely on the image data, we can train the network on an anisotropic dataset and get impressive results on an isotropic dataset. Figure 7 shows the receiver operating characteristic (ROC) curve for all four datasets.

TODO - ADD QUALITATIVE RESULTS

5.3. Graph Based Strategies

TODO - QUANTIFY IMPROVEMENT BY MULTI-CUT - READERS CAN SKIP SECTION FOR NOW

Using a graph-based optimization strategy prevents XX segments from merging compared to the simple hierarchical agglomeration strategy with an optimal threshold cut off. Since correcting merge errors is significantly more difficult than correcting split errors, it is desirable to limit the number of false merges. The graph-based strategies significantly improve this error type.

5.4. Variation of Information Improvements

We compute the variation of information for our segmentations against the expert-labeled ground truth datasets. The input segmentation to our network serves as a baseline. We evaluate NeuroProof (our input) at several different thresholds to create a variation of information curve. Similarly, we run the greedy-additive heuristic with varying parameters that increase the probability needed for merging nodes. Figure 8 shows the results on the datasets compared to the baseline (green) and an oracle (blue). The oracles sees the entire constructed graph from our algorithm and correctly partitions the graph based on the ground truth. Our methods decreases the split variation of information by a factor of XX% and only increases the merge variation of information by a factor of XX% on the test datasets. Table 4 pro-

Dataset	VI Split	VI Merge
Kasthuri Training		
Kasthuri Testing		
FlyEM Vol. 1		
FlyEM Vol. 2		

Table 4: Variation of Information Change

vides a quantitative overview for the changes in variation of information.

TODO - ADD QUALITATIVE RESULTS

6. Conclusions

We present a novel method for framework neuronal processes in connectomics image datasets. We extend on top of existing region-based agglomeration strategies and show significant accuracy improvement on two datasets from two different species. By extracting skeletons from every segment in the input we can quickly produce a graph G with N nodes and E weighted edges from the input. We populate the edge weights using a 3-D CNN that, unlike previous methods, does not use the raw image data. Separating the neural network from the images allows us to train on anisotropic data and test on isotropic data with different sample resolution. This is exceptionally important in connectomics because of the extreme labor-intensive cost of manually segmenting ground truth data. We use existing graph partitioning strategies on the G , enabling us to enforce domain-constraints on the resulting segmentation. For us, our constraints follow from the topology of neurons. However, this framework extends to other domains with varying constraints.

References

- [1] B. Andres, T. Kroege, K. L. Briggman, W. Denk, N. Korogod, G. Knott, U. Koethe, and F. A. Hamprecht. Globally optimal closed-surface segmentation for connectomics. In *European Conference on Computer Vision*, pages 778–791. Springer, 2012. 2, 3
- [2] J. A. Bogovic, G. B. Huang, and V. Jain. Learned versus hand-designed feature representations for 3d agglomeration. *arXiv preprint arXiv:1312.6159*, 2013. 2
- [3] K. Briggman, W. Denk, S. Seung, M. N. Helmstaedter, and S. C. Turaga. Maximin affinity learning of image segmentation. In *Advances in Neural Information Processing Systems*, pages 1865–1873, 2009. 2
- [4] K. Chatfield, K. Simonyan, A. Vedaldi, and A. Zisserman. Return of the devil in the details: Delving deep into convolutional nets. *arXiv preprint arXiv:1405.3531*, 2014. 2, 4
- [5] D. Ciresan, A. Giusti, L. M. Gambardella, and J. Schmidhuber. Deep neural networks segment neuronal membranes in electron microscopy images. In *Advances in neural information processing systems*, pages 2843–2851, 2012. 2

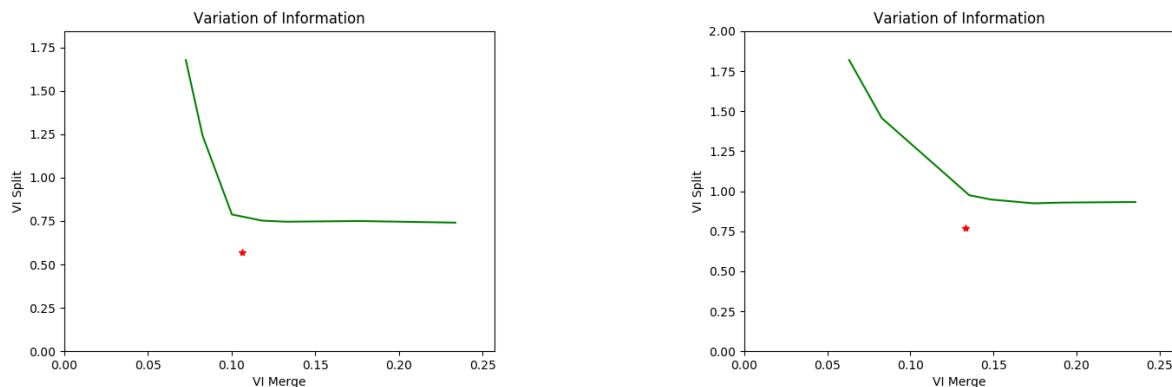


Figure 8: The improvement on variation of information from the baseline NeuroProof segmentation (green). Results closer to the origin are better.

- [6] E. D. Demaine, D. Emanuel, A. Fiat, and N. Immerlica. Correlation clustering in general weighted graphs. *Theoretical Computer Science*, 361(2-3):172–187, 2006. 3
- [7] K.-I. Funahashi. On the approximate realization of continuous mappings by neural networks. *Neural networks*, 2(3):183–192, 1989. 4
- [8] X. Glorot and Y. Bengio. Understanding the difficulty of training deep feedforward neural networks. In *Proceedings of the Thirteenth International Conference on Artificial Intelligence and Statistics*, pages 249–256, 2010. 6
- [9] D. Haehn, J. Hoffer, B. Matejek, A. Suissa-Peleg, A. K. Al-Awami, L. Kamensky, F. Gonda, E. Meng, W. Zhang, R. Schalek, et al. Scalable interactive visualization for connectomics. In *Informatics*, volume 4, page 29. Multidisciplinary Digital Publishing Institute, 2017.
- [10] D. Haehn, V. Kaynig, J. Tompkin, J. W. Lichtman, and H. Pfister. Guided proofreading of automatic segmentations for connectomics. *arXiv preprint arXiv:1704.00848*, 2017. 3
- [11] D. Haehn, S. Knowles-Barley, M. Roberts, J. Beyer, N. Kasthuri, J. W. Lichtman, and H. Pfister. Design and evaluation of interactive proofreading tools for connectomics. *IEEE Transactions on Visualization and Computer Graphics*, 20(12):2466–2475, 2014.
- [12] D. G. C. Hildebrand, M. Cicconet, R. M. Torres, W. Choi, T. M. Quan, J. Moon, A. W. Wetzel, A. S. Champion, B. J. Graham, O. Randlett, et al. Whole-brain serial-section electron microscopy in larval zebrafish. *Nature*, 545(7654):345–349, 2017. 1
- [13] A. Horňáková, J.-H. Lange, and B. Andres. Analysis and optimization of graph decompositions by lifted multicuts. In *International Conference on Machine Learning*, pages 1539–1548, 2017. 3
- [14] V. Jain, B. Bollmann, M. Richardson, D. Berger, M. Helmstädt, K. Briggman, W. Denk, J. Bowden, J. Mendenhall, W. Abraham, K. Harris, N. Kasthuri, K. Hayworth, R. Schalek, J. Tapia, J. Lichtman, and S. Seung. Boundary learning by optimization with topological constraints. In *Proc. IEEE CVPR 2010*, pages 2488–2495, 2010. 2
- [15] M. Januszewski, J. Maitin-Shepard, P. Li, J. Kornfeld, W. Denk, and V. Jain. Flood-filling networks. *arXiv preprint arXiv:1611.00421*, 2016. 2
- [16] J. H. Kappes, M. Speth, G. Reinelt, and C. Schnörr. Higher-order segmentation via multicuts. *Computer Vision and Image Understanding*, 143:104–119, 2016. 3
- [17] N. Kasthuri, K. J. Hayworth, D. R. Berger, R. L. Schalek, J. A. Conchello, S. Knowles-Barley, D. Lee, A. Vázquez-Reina, V. Kaynig, T. R. Jones, et al. Saturated reconstruction of a volume of neocortex. *Cell*, 162(3):648–661, 2015. 1, 4
- [18] V. Kaynig, A. Vazquez-Reina, S. Knowles-Barley, M. Roberts, T. R. Jones, N. Kasthuri, E. Miller, J. Lichtman, and H. Pfister. Large-scale automatic reconstruction of neuronal processes from electron microscopy images. *Medical image analysis*, 22(1):77–88, 2015. 2
- [19] B. W. Kernighan and S. Lin. An efficient heuristic procedure for partitioning graphs. *The Bell system technical journal*, 49(2):291–307, 1970.
- [20] M. Keuper, E. Levinkov, N. Bonneel, G. Lavoué, T. Brox, and B. Andres. Efficient decomposition of image and mesh graphs by lifted multicuts. In *Proceedings of the IEEE International Conference on Computer Vision*, pages 1751–1759, 2015. 3, 4
- [21] S. Knowles-Barley, V. Kaynig, T. R. Jones, A. Wilson, J. Morgan, D. Lee, D. Berger, N. Kasthuri, J. W. Lichtman, and H. Pfister. Rhoanet pipeline: Dense automatic neural annotation. *arXiv preprint arXiv:1611.06973*, 2016. 1, 2
- [22] S. Knowles-Barley, V. Kaynig, T. R. Jones, A. Wilson, J. Morgan, D. Lee, D. Berger, N. Kasthuri, J. W. Lichtman, and H. Pfister. Rhoanet pipeline: Dense automatic neural annotation, 2016. (available on arXiv:1611.06973 [cs.CV]). 2
- [23] K. Lee, A. Zlateski, V. Ashwin, and H. S. Seung. Recursive training of 2d-3d convolutional networks for neuronal boundary prediction. In *Advances in Neural Information Processing Systems*, pages 3573–3581, 2015. 1, 2

- [24] A. L. Maas, A. Y. Hannun, and A. Y. Ng. Rectifier nonlinearities improve neural network acoustic models. In *Proc. ICML*, volume 30, 2013. 2, 4
- [25] M. Meila. Comparing clusterings by the variation of information. In *Colt*, volume 3, pages 173–187. Springer, 2003. 6
- [26] Y. Nesterov. A method of solving a convex programming problem with convergence rate $o(1/k^2)$. 2, 4
- [27] J. Nunez-Iglesias, R. Kennedy, S. M. Plaza, A. Chakraborty, and W. T. Katz. Graph-based active learning of agglomeration (gala): a python library to segment 2d and 3d neuroimages. *Frontiers in neuroinformatics*, 8, 2014. 1, 2
- [28] T. Parag, A. Chakraborty, S. Plaza, and L. Scheffer. A context-aware delayed agglomeration framework for electron microscopy segmentation. *PLOS ONE*, 10(5):1–19, 05 2015. 1, 2, 5
- [29] T. Parag, F. Tschopp, W. Grisaitis, S. C. Turaga, X. Zhang, B. Matejek, L. Kamensky, J. W. Lichtman, and H. Pfister. Anisotropic em segmentation by 3d affinity learning and agglomeration. *arXiv preprint arXiv:1707.08935*, 2017. 1, 2
- [30] D. Rolnick, Y. Meirovitch, T. Parag, H. Pfister, V. Jain, J. W. Lichtman, E. S. Boyden, and N. Shavit. Morphological error detection in 3d segmentations. *arXiv preprint arXiv:1705.10882*, 2017. 3
- [31] O. Ronneberger, P. Fischer, and T. Brox. U-net: Convolutional networks for biomedical image segmentation. In *International Conference on Medical Image Computing and Computer-Assisted Intervention*, pages 234–241. Springer, 2015. 1, 2, 5
- [32] M. Sato, I. Bitter, M. A. Bender, A. E. Kaufman, and M. Nakajima. Teasar: Tree-structure extraction algorithm for accurate and robust skeletons. In *Computer Graphics and Applications, 2000. Proceedings. The Eighth Pacific Conference on*, pages 281–449. IEEE, 2000. 3
- [33] P. Schlegel, M. Costa, and G. S. Jefferis. Learning from connectomics on the fly. *Current Opinion in Insect Science*, 2017. 5
- [34] J. Shi and J. Malik. Normalized cuts and image segmentation. *IEEE Transactions on pattern analysis and machine intelligence*, 22(8):888–905, 2000. 3
- [35] S.-y. Takemura, Y. Aso, T. Hige, A. Wong, Z. Lu, C. S. Xu, P. K. Rivlin, H. Hess, T. Zhao, T. Parag, et al. A connectome of a learning and memory center in the adult drosophila brain. *Elife*, 6, 2017. 4, 5
- [36] S. Tatiraju and A. Mehta. Image segmentation using k-means clustering, em and normalized cuts. *Department of EECS*, 1:1–7, 2008. 3
- [37] S. Turaga, K. Briggman, M. Helmstaedter, W. Denk, and S. Seung. Maximin affinity learning of image segmentation. In *Advances in Neural Information Processing Systems 22*. 2009. 5
- [38] A. Vázquez-Reina, M. Gelbart, D. Huang, J. Lichtman, E. Miller, and H. Pfister. Segmentation fusion for connectomics. In *Proc. IEEE ICCV*, pages 177–184, Nov 2011. 2
- [39] N. M. Zaitoun and M. J. Aqel. Survey on image segmentation techniques. *Procedia Computer Science*, 65:797–806, 2015. 2
- [40] T. Zhao and S. M. Plaza. Automatic neuron type identification by neurite localization in the drosophila medulla. *arXiv preprint arXiv:1409.1892*, 2014. 3
- [41] A. Zlateski and H. S. Seung. Image segmentation by size-dependent single linkage clustering of a watershed basin graph. *arXiv preprint arXiv:1505.00249*, 2015. 1, 2, 5
- [42] J. Zung, I. Tartavull, and H. S. Seung. An error detection and correction framework for connectomics. *CoRR*, abs/1708.02599, 2017. 3

918
919
920
921
922
923
924
925
926
927
928
929
930
931
932
933
934
935
936
937
938
939
940
941
942
943
944
945
946
947
948
949
950
951
952
953
954
955
956
957
958
959
960
961
962
963
964
965
966
967
968
969
970
971